Incommensurability-induced sub-ballistic narrow-band-states in twisted bilayer graphene

Miguel Gonçalves,[1] Hadi Z. Olyaei,[1] Bruno Amorim,[2] Rubem Mondaini,[3] Pedro Ribeiro,[1, 3] and Eduardo V. Castro[4, 3]

[1] *CeFEMA, Instituto Superior Técnico, Universidade de Lisboa, Av. Rovisco Pais, 1049-001 Lisboa, Portugal*
[2] *Centro de Física das Universidades do Minho e Porto,*
University of Minho, Campus of Gualtar, 4710-057, Braga, Portugal
[3] *Beijing Computational Science Research Center, Beijing 100193, China*
[4] *Centro de Física das Universidades do Minho e Porto,*
Departamento de Física e Astronomia, Faculdade de Ciências,
Universidade do Porto, 4169-007 Porto, Portugal

We study the localization properties of electrons in incommensurate twisted bilayer graphene for small angles, encompassing the narrow-band regime, by numerically exact means. Sub-ballistic states are found within the narrow-band region around the magic angle. Such states are delocalized in momentum-space and follow non-Poissonian level statistics, in contrast with their ballistic counterparts found for close commensurate angles. Transport results corroborate this picture: for large enough systems, the conductance decreases with system size for incommensurate angles within the sub-ballistic regime. Our results show that incommensurability/quasiperiodicity effects are of crucial importance in the narrow-band regime. The incommensurate nature of a general twist angle must therefore be taken into account for an accurate description of magic-angle twisted bilayer graphene.

Narrow-band electronic systems are natural platforms to search for exotic physics. Otherwise modest perturbations can here attain energies comparable to the bandwidth, yielding a non-perturbative reorganization of the eigenstates into phases of matter often very different from their parent state. Recently, twisted bilayer graphene (tBLG) has emerged as a paradigmatic system displaying this mechanism. When the twist angle between the layers approaches the so-called *magic angle,* $\theta \approx 1.1°$, extremely narrow, nearly flat, bands appear at low energies [1–6]. In this regime, superconductivity [7] and correlated insulating phases [8] were observed around integer electronic fillings, pointing to relevant electron-electron interactions [9]. The similarities with the cuprates [10] sparked redoubled interest in these effects, which emerge here in a simpler, cleaner and highly tunable system, where all ingredients can potentially be easily isolated and understood. This triggered intense theoretical [11–27] and experimental [28–37] research.

Due to the high degree of sample-purity, models of tBLG typically assume a Fermi gas with a flat-band dispersion as a starting point [11–13, 18, 21, 23–25, 38, 39]. This is a major difference with respect to the cuprates, as disorder is intrinsic to doped Mott insulators [40] and has even been observed to increase the critical temperature [41].

Nonetheless, in Refs. [42, 43], localization has been predicted for the recently observed "dodecagonal graphene quasicrystal" [44, 45], a tBLG with $\theta = 30°$. This phenomenon is due to the quasiperiodic nature of the system for incommensurate values of θ. Incommensurability was also shown to induce quantum phase transitions in two-dimensional (2d) models [46], including the so-called chiral limit of tBLG for moderate twist angles ($\theta \simeq 9°$),

yielding a critical "magic-angle semimetallic" state with a multifractal momentum-space wave function. For more realistic models of tBLG, the proximity to commensurate angles with small unit cells, has been shown to imprint sharp conductance signatures [47]. However, for small angles, $\theta \lesssim 3°$, these features seem to be washed away, in accordance with the general belief underlying continuous models [14].

Incommensurability can doubtlessly induce localization [48–50] or multifractallity in 2d [46]. However, at this point, it is not clear how the commensurate/incommensurate nature of the tBLG structure affects the properties of eigenstates in the small-angle narrow-band regime. As in tBLG several energy scales are comparable, understanding the role played by incommensurability is essential to devise effective interacting models able to faithfully capture their competition.

In this letter we address the effects of incommensurability/quasiperiodicity in the nature of the narrow-band states and on the transport properties of tBLG, neglecting electron-electron interactions. We employ a number of numerically exact methods to show that incommensurate angles induce momentum-space delocalization of the narrow-band states, whereas for commensurate angles eigenstates are ballistic with a localized momentum-space wave function. The presence of a sub-ballistic regime is corroborated by finite-size scaling analysis of the conductance which decreases with system size for incommensurate structures, while saturating for commensurate ones.
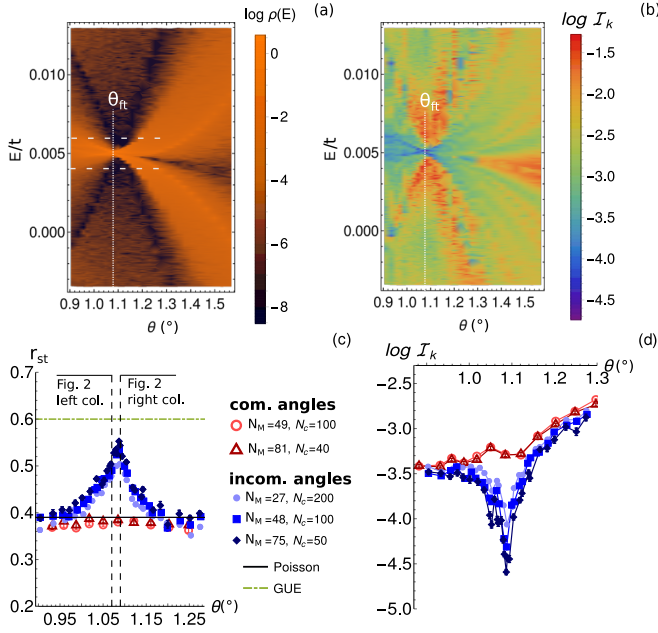
FIG. 1. (a,b) DOS, ρ, and momentum-space inverse participation ratio, $\mathcal{I}_k$, for incommensurate structures and variable θ. The system sizes range between $N = 2 \times 10^5 - 8 \times 10^5$ sites, $N_{\mathrm{M}} = 48$ moiré cells and an average over $N_c = 100$ realizations was performed. (c,d) Level spacing, r_{st}, and $\mathcal{I}_k$ averaged over the energy window between dashed line in (a), computed both for a set of commensurate angles (variable m, $r = 1$, $n = 7, 9$) and incommensurate angles (variable m, $r = 9, 12, 15$, $n = 1$), for system sizes going up to more than $N = 10^6$ ($N_{\mathrm{M}} = 81$ and $N_{\mathrm{M}} = 75$).
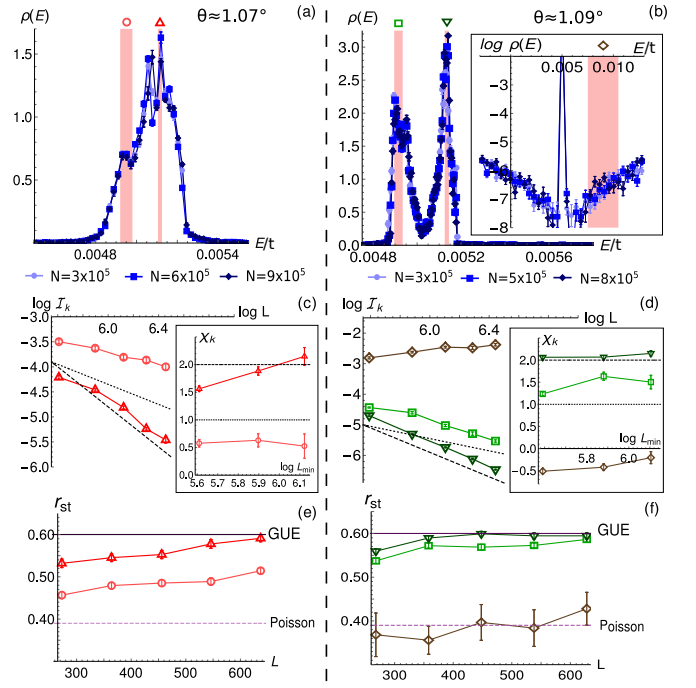

FIG. 2. (a,b) DOS for incommensurate structures of different sizes, for the angles marked in Fig. 1(c). The inset in (b) shows a log-scale plot of $\rho(E)$ for a wider energy range. (c-f) Average r_{st} and $\mathcal{I}_k$ for a small energy window around selected energies, indicated by the shaded areas in (a,b) along with marker on top, as a function of the linear system size $L \propto N^{1/2}$ (the largest systems correspond to $N \gtrsim 10^6$, see [51]). The dotted and dashed lines in (c,d) correspond respectively to $\mathcal{I}_k \sim L^{-1}, L^{-2}$. The insets in (c,d) contain the quantity $\chi_k = -d \log \mathcal{I}_k / d \log L$, computed by fitting the data points $(\log L, \log \mathcal{I}_k)$, considering only points with $L \geq L_{\min}$. Complete information on the data used in Figs. (a-f) can be found in table S1 in [51].

Model and Methods.— We study a model of tBLG with the tight-binding Hamiltonian

$$H = -t \sum_{l, \langle \mathbf{r}_{l,A}, \mathbf{r}_{l,B} \rangle} c_{l,A}^{\dagger}(\mathbf{r}_{l,A}) c_{l,B}(\mathbf{r}_{l,B})$$
$$+ \sum_{|\mathbf{r}_{1,\alpha} - \mathbf{r}_{2,\beta}| < \Lambda} t_{\perp}(|\mathbf{r}_{1,\alpha} - \mathbf{r}_{2,\beta}|) c_{1,\alpha}^{\dagger}(\mathbf{r}_{1,\alpha}) c_{2,\beta}(\mathbf{r}_{2,\beta}) + \mathrm{h.c.},$$

(1)

where the first term describes the nearest-neighbor intralayer hopping t [52], and $l = 1, 2$ is the layer index. The second term models the interlayer hopping, with $\mathbf{r}_{l,\alpha}$ the in-plane position in layer l and sublattice $\alpha = A, B$. The interlayer hopping $t_{\perp}(r)$ is parameterized in terms of Slater-Koster parameters used in Refs. [53–55]: $r_{\triangle}^2 t_{\perp}(r) = d_{\perp}^2 V_{pp\sigma}(r_{\triangle}) + r^2 V_{pp\pi}(r_{\triangle})$ where $r_{\triangle} = \sqrt{d_{\perp}^2 + r^2}$, $V_{pp\sigma}(r) = t_{\perp} \exp[(d_{\perp} - r)/\delta]$, $V_{pp\pi}(r) = -t \exp[(d - r)/\delta]$, $d = 0.142 \, \mathrm{nm}$ is the C-C distance, $d_{\perp} = 0.335 \, \mathrm{nm}$ is the distance between layers and $\delta = 0.184a$, with $a = 0.246 \, \mathrm{nm}$ the monolayer lattice constant. We used $t = 2.7 \, \mathrm{eV}$ and $t_{\perp} = 0.48 \, \mathrm{eV}$. For the calculations presented hereafter, energy and length scales are measured in units of t and a, respectively.

Interlayer hoppings were considered only among atoms with in-plane distance $r < \Lambda$. For a small cutoff, $\Lambda \sim d$,

the narrow-band angle, θ_{ft}, is very sensitive to relative translations of the layers. This effect washes-away for larger Λ. To mitigate finite-size effects we set $\Lambda = 2.6d$, above which our numerical results remained unchanged.

A tBLG lattice with periodic boundary conditions can be defined by the integers (m, r, n), where (m, r) are coprime numbers that determine the commensurate twist angle $\theta(m, r)$ [3], and n is the linear number of supercells in the system, i.e., the lattice contains n^2 supercells. The superlattice basis vectors, the commensurate twist angle $\theta(m, r)$ [3], and the number of moiré pattern cells $N_{\mathrm{M}}(n, r)$ as a function of the integer tuples are given in the supplemental material (SM) [51]. We follow a well established method that consists of approximating an infinite incommensurate structure (here characterised by twist angle θ_{ic}) by a sequence of approximants with increasing lattice size (here taken to be $n = 1$ structures with $\theta(m, r) \simeq \theta_{\mathrm{ic}}$) [56]. An approximant structure may encompass many moiré cells (for $r_i \neq 1$), its unit cell coincides with the size of the system. Commensurate

structures are obtained by taking $n > 1$ and a finite-size scaling analysis is performed by increasing n with fixed (m, r). The main advantage of this method is to eliminate boundary effects, present for open systems, by always considering closed boundary conditions [57].

To characterize the system's eigenstates near the narrow-band energies, we used Krylov-Schur exact diagonalization (ED) with shift-invert [58, 59]. To further mitigate finite-size effects, we average all relevant quantities with respect to a phase-twist we introduce in the boundary conditions and to a random relative stacking translation, $\boldsymbol{\delta}_t$, between the two layers. We approximate the density of states (DOS) by binning the energies, $\rho(E_i) = N_s(E_i)/(\Delta E N)$, where $N_s(E_i)$ is the number of states inside the bin centered around energy E_i and width ΔE, and N is the total number of sites. We also study the eigenstates' momentum-space localization properties through the momentum-space inverse participation ratio (IPR_k) [60],

$$\mathcal{I}_k = \left(\sum_{\boldsymbol{k}, \alpha} |\Psi_{l, \boldsymbol{k}, \alpha}|^2 \right)^{-2} \sum_{\boldsymbol{k}, \alpha} |\Psi_{l, \boldsymbol{k}, \alpha}|^4, \quad (2)$$

where $\Psi_{l, \boldsymbol{k}, \alpha}$ is the eigenstate amplitude in layer l momentum $\boldsymbol{k}$ and sublattice α. For wavefunctions localized in momentum-space, $\mathcal{I}_k \sim L^0$, where L is the linear system size [61], whereas a $\mathcal{I}_k \sim L^{-\nu}$, with $\nu > 0$, indicates momentum-space delocalization. We checked that the real-space inverse participation ratio always scales with L^{-2}, signaling no real-space localization. Therefore, $\mathcal{I}_k \sim L^{-\nu}$, with $\nu > 0$, indicates the presence of sub-ballistic states.

To complement the eigenstate's analysis, we study the statistics of the energy levels through the quantity $r_{\text{st}} = \langle r_i \rangle_{E \in E_w, N_c}$, where r_i is defined as $r_i = \min(\Delta E_i, \Delta E_{i+1}) / \max(\Delta E_i, \Delta E_{i+1})$, with $\Delta E_i = E_i - E_{i-1}$ (for ordered levels $E_i > E_{i-1}$) and where the average, $\langle ... \rangle_{E \in E_w, N_c}$, is first performed over all the eigenvalues within an energy window E_w for each realization and then over N_c realizations of boundary twists and stacking shifts. The relevant known values [62] for r_{st} are: (i) $r_{\text{st}}^{\text{Poisson}} \approx 0.39$ if the spacings follow a Poisson distribution; (ii) $r_{\text{st}}^{\text{GUE}} \approx 0.6$ for the Gaussian unitary ensemble (GUE), when the Hamiltonian breaks time-reversal symmetry (here due to twisted boundary conditions). Case (i) applies when the wavefunction is localized in some basis: this includes ballistic (momentum-space localized) or insulating (real-space localized) states. Case (ii) applies when the wavefunction is delocalized in any basis.

Finally, we analyze transport properties by computing the conductance, G. We considered two semi-infinite stripes of single-layer graphene that overlap within a region of fixed width and variable length, $\sim L$. The graphene leads are rendered metallic by doping (see SM [51] for more details).

Commensurate vs. incommensurate.— We start by providing a general overview on the differences between commensurate and incommensurate structures around the first magic-angle. Fig. 1(a,b), depict the DOS and $\mathcal{I}_k$ of incommensurate structures for different energies and angles with a fixed number of moiré cells $N_M = 48$. As expected, a narrow-band occurs for the *magic-angle* $\theta_{\text{ft}} \approx 1.09°$, close to the merging of two van-Hove singularities (VHS) present at larger θ. Remarkably, Fig. 1(b) shows that $\mathcal{I}_k$ becomes very small for energies within the narrow-band. This is not observed for commensurate structures, as justified below.

Figs. 1(c,d) show r_{st} and $\mathcal{I}_k$ averaged within the energy window represented by the horizontal dashed lines in Fig. 1(a), both for incommensurate ($r = 9, 12, 15$; $n = 1$) and commensurate ($r = 1$; $n = 7, 9$) structures. As expected for ballistic states, for commensurate angles, r_{st} follows Poisson statistics and $\mathcal{I}_k$ is independent of the system size. Conversely, for incommensurate angles: (i) r_{st} raises above the Poisson value within a finite interval of (incommensurate) angles, reaching a maximum value for $\theta = \theta_{\text{ft}}$; (ii) For the same interval of angles, $\mathcal{I}_k$ scales down with system size, reaching a minimum for $\theta = \theta_{\text{ft}}$. Outside this regime, $\mathcal{I}_k$ becomes L-independent and approaches the value obtained for commensurate structures [Fig. 1(d)].

These results suggest that, as a function of θ, there is a "collision" of energy bands around θ_{ft}, with subsequent band inversion. We confirm such phenomena when the narrow band regime is tuned by changing the amplitude of $t_\perp$ (see [51]). It is plausible that the same happens when changing θ (for fixed $t_\perp$), but a similar analysis is prevented within our setup by changes in system size with θ. Within this picture, the narrow-band regime corresponds to the collision area where states from the two bands become highly mixed (as seen by $\mathcal{I}_k$) and their energy levels repel (as seen by r_{st}). Moreover, at least a finite portion of the states inside the considered energy window have sub-ballistic properties within a finite interval of angles that we now explore in more detail.

Sub-ballistic regime.— We provide an energy resolved and finite-size scaling analysis. Figure 2 shows two angles chosen in order to observe merged VHSs in 2(a), and a minimal bandwidth in 2(b).

Figure 2(c,d) and 2(e,f) depict, respectively, $\mathcal{I}_k$ and r_{st} averaged over the shaded energy windows of Figs. 2(a,b). The approximant series was chosen to ensure a monotonic approach to the desired incommensurate angle upon increasing system size (see [51]), and we ensure an overall angle variation in the series below $10''$. States with different scaling behaviors arise at different energies. Typically, when $\rho(E)$ is larger, the $\mathcal{I}_k$ is smaller and decreases faster with system size. The latter correlates with a faster scaling of r_{st} towards the GUE value. For instance, for energies corresponding to the larger DOS observed in Fig. 2(b), $\mathcal{I}_k$ reaches its smallest value, scal-
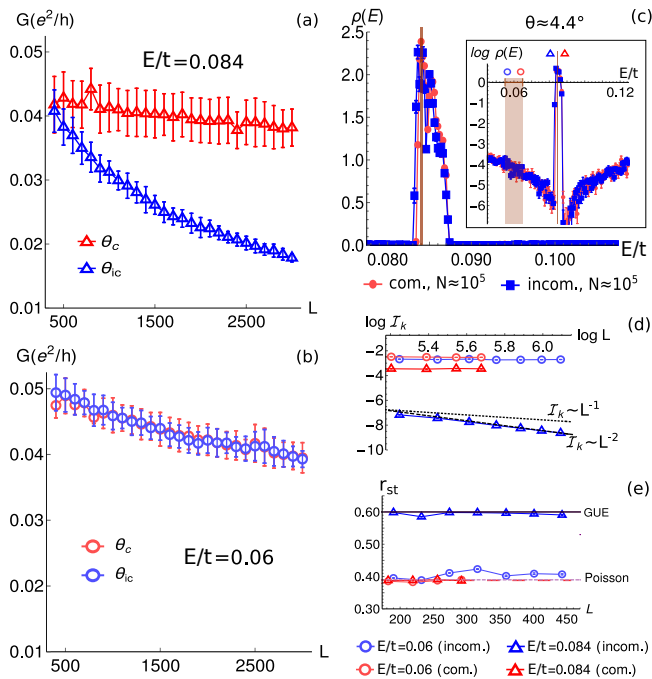
FIG. 3. (a,b) Finite-size scaling analysis of the conductance for commensurate, θ_c, and incommensurate, θ_{ic}, angles near θ_{ft}: (a) is for $E = 0.084$, inside the narrow band; while (b) is for $E = 0.06$, outside. The error bars correspond to the error of the average conductance computed for 25 different stackings between the graphene layers (see [51]). (c) DOS for θ_c and θ_{ic}. Inset: log-scale plot for a wider energy range. (d,e) Finite-size analysis of $\mathcal{I}_k$ and r_{st}, averaged on small energy windows [shaded areas in (c) around $E = 0.06$ and $E = 0.084$, with widths $\Delta E = 10^{-2}$ and 2×10^{-4}] for θ_c, and θ_{ic} (see table S2 in [51]). For $E = 0.06$, the DOS is small and a larger energy window is used to increase statistics. Plotmarkers are used in the scaling analysis of (d,e). Dotted and dashed lines in (d) correspond respectively to $\mathcal{I}_k \sim L^{-1}, L^{-2}$.

ing as $\mathcal{I}_k \sim L^{-2}$, and r_{st} converges very quickly with L into the GUE value. For other energies within the narrow-band, we generically have $0 < \chi_k < 2$, where $\chi_k = -d\log\mathcal{I}_k/d\log L$, and $r_{st}^{Poisson} < r_{st} < r_{st}^{GUE}$. Even if there are considerable finite-size effects, as χ_k and r_{st} still seem to be increasing with L up to the sizes we can reach (see Fig. 2), it is clear that states in this region are sub-ballistic. These findings are further corroborated by the transport results of the next section.

Outside the narrow-band region, states are ballistic ($r_{st} = r_{st}^{Poisson}$ and $\mathcal{I}_k \sim L^0$) even in regions with a highly suppressed DOS. An example is given in Fig. 2(f) for the states within the shaded area in the inset of Fig. 2(b).

Finally, for angles above and below the narrow-band regime in Fig. 2, but still within the sub-ballistic range, states exhibiting non-ballistic properties are also observed. However, their limiting behavior is less conclusive (see [51]).

Conductance.— In order to understand the consequences of the sub-ballistic states in transport, we computed the conductance, G. Unfortunately, for the parameters above, finite-size effects are too severe to draw systematic conclusions (see SM [51]), as the largest systems attainable contain only $N_M \sim 10^2$ moiré cells. To mitigate finite-size effects by increasing the number of moiré cells simulated, we increased the interlayer coupling to $t_\perp = 1.9$ eV, a well-known procedure for shifting the narrow-band regime to larger angles ($\theta_{ft} \sim 4.4°$, in this case), with smaller period moiré patterns [1–3]. Representative conductance results for $t_\perp = 1.9$ eV are given in Figs. 3(a,b), together with an ED analysis in Figs. 3(c-e). In Fig. 3(a), $G(L)$ is computed for an energy within the narrow-band. In the commensurate case, $G(L)$ converges with L as expected. Conversely, it decreases with L in the incommensurate case, hinting sub-ballistic transport. For smaller L, the conductance is very similar in both cases, showing that large enough systems are crucial to observe incommensurability effects in the conductance. On the other hand, ED captures a sub-ballistic behavior even for the smaller systems used: a small, L-decreasing $\mathcal{I}_k$ and GUE statistics are observed in Figs. 3(d,e).

For energies outside the narrow-band, where the DOS is very small [see inset in Fig. 3(c)], the ED and conductance results are very similar for commensurate and incommensurate angles [Figs. 3(b,d)], suggesting that incommensurability effects become unimportant.

Discussion.— We studied the eigenstate localization and transport properties of tBLG for commensurate and incommensurate angles around the first magic angle. For a finite interval of incommensurate angles, encompassing the narrow-band regime, eigenstate delocalization in momentum-space is concomitant with non-Poisson energy level statistics and with a decrease of the conductance with system size. This is compatible with sub-ballistic transport and contrasts with commensurate angles, or with angles away from the narrow-band region, where transport is ballistic. Moreover, the scaling of $\mathcal{I}_k$ with system size seem to indicate diffusive behavior, although the results from conductance scaling are unclear with the available system sizes. The present results indicate that the scenario of a "magic angle semimetal" with momentum-space delocalized wave functions, proposed in Ref. [46] for a model of moderate angle chiral tBLG, extends to models of incommensurate tBLG with twist angles close to the experimentally relevant magic angle $\theta \approx 1.1°$.

Our results have major implications for the low energy properties of tBLG as, in the narrow-band regime, incommensurability alone breaks down a Bloch wave description even for perfectly clean samples. In particular, an analysis of the influence of correlations should equally account for the incommensurate nature of tBLG. These effects have been overlooked in the vast majority of theoretical studies on tBLG, namely the ones starting from continuum models [1–3]. Our findings may also be relevant to the enhanced, linear temperature resistivity ob-

served in tBLG at the magic angle [63, 64]. Even though we restricted the study to small angle tBLG, we anticipate that the present results also apply to other systems with concomitant narrow-bands and incommensurability: tBLG at large angles [65], double bilayers [66–68], twisted bilayers of transition metal dichalcogenides [69, 70]. We also note that even though our model does not account for lattice relaxation, recent experimental results showed that near the magic-angle, both the relaxed and unrelaxed structures are stable, being possible to change between them by applying a STM tip pulse [71]. Moreover, even in the relaxed case, the narrow-band is still present [72] and may even be narrower [73] with incommensurability effects possibly enhanced.

As single-particle localization can give rise to many-body localization once interactions are included [74, 75], we expect the single-particle properties here reported to also play an important role once interactions are considered.

Finally, we checked that our results are robust to relatively strong Anderson-like disorder (of the order of the narrow-band's width, see [51]). Interestingly, commensurate structures are more fragile and, at stronger disorder, their properties approach those of disorder-free incommensurate structures.

[1] J. M.B. Lopes Dos Santos, N. M.R. Peres, and A. H. Castro Neto, "Graphene bilayer with a twist: Electronic structure," Phys. Rev. Lett. **99**, 256802 (2007), arXiv:0704.2128.

[2] Rafi Bistritzer and Allan H. MacDonald, "Moiré bands in twisted double-layer graphene," Proc. Natl. Acad. Sci. U. S. A. **108**, 12233–12237 (2011), arXiv:1009.4203.

[3] J. M.B. Lopes Dos Santos, N. M.R. Peres, and A. H. Castro Neto, "Continuum model of the twisted graphene bilayer," Phys. Rev. B - Condens. Matter Mater. Phys. **86**, 155449 (2012).

[4] G. De Trambly Laissardière, D. Mayou, and L. Magaud, "Localization of dirac electrons in rotated graphene bilayers," Nano Lett. **10**, 804–808 (2010), arXiv:0904.1233.

[5] E. Suárez Morell, J. D. Correa, P. Vargas, M. Pacheco, and Z. Barticevic, "Flat bands in slightly twisted bilayer graphene: Tight-binding calculations," Phys. Rev. B - Condens. Matter Mater. Phys. **82**, 121407 (2010), arXiv:1012.4320.

[6] S. Shallcross, S. Sharma, E. Kandelaki, and O. A. Pankratov, "Electronic structure of turbostratic graphene," Phys. Rev. B - Condens. Matter Mater. Phys. **81**, 165105 (2010), arXiv:0910.5811.

[7] Yuan Cao, Valla Fatemi, Shiang Fang, Kenji Watanabe, Takashi Taniguchi, Efthimios Kaxiras, and Pablo Jarillo-Herrero, "Unconventional superconductivity in magic-angle graphene superlattices," Nature **556**, 43–50 (2018), arXiv:1803.02342.

[8] Yuan Cao, Valla Fatemi, Ahmet Demir, Shiang Fang, Spencer L. Tomarken, Jason Y. Luo, Javier D. Sanchez-Yamagishi, Kenji Watanabe, Takashi Taniguchi, Efthimios Kaxiras, Ray C. Ashoori, and Pablo Jarillo-Herrero, "Correlated insulator behaviour at half-filling in magic-angle graphene superlattices," Nature **556**, 80–84 (2018), arXiv:1802.00553.

[9] Leon Balents, Cory R. Dean, Dmitri K. Efetov, and Andrea F. Young, "Superconductivity and strong correlations in moiré flat bands," Nat. Phys. **16**, 725–733 (2020).

[10] J. G. Bednorz and K. A. Müller, "Possible high Tc superconductivity in the Ba-La-Cu-O system," Zeitschrift für Phys. B Condens. Matter **64**, 189–193 (1986).

[11] Jian Kang and Oskar Vafek, "Symmetry, Maximally Localized Wannier States, and a Low-Energy Model for Twisted Bilayer Graphene Narrow Bands," Phys. Rev. X **8**, 031088 (2018).

[12] Liujun Zou, Hoi Chun Po, Ashvin Vishwanath, and T. Senthil, "Band structure of twisted bilayer graphene: Emergent symmetries, commensurate approximants, and Wannier obstructions," Phys. Rev. B **98**, 085435 (2018), arXiv:1806.07873.

[13] Hoi Chun Po, Liujun Zou, Ashvin Vishwanath, and T. Senthil, "Origin of Mott Insulating Behavior and Superconductivity in Twisted Bilayer Graphene," Phys. Rev. X **8**, 031089 (2018), arXiv:1803.09742.

[14] Grigory Tarnopolsky, Alex Jura Kruchkov, and Ashvin Vishwanath, "Origin of Magic Angles in Twisted Bilayer Graphene," Phys. Rev. Lett. **122**, 106405 (2019), arXiv:1808.05250.

[15] Fatemeh Haddadi, Quan Sheng Wu, Alex J. Kruchkov, and Oleg V. Yazyev, "Moiré Flat Bands in Twisted Dou-

ble Bilayer Graphene," Nano Lett. **20**, 2410–2415 (2020), arXiv:1906.00623.

[16] Zhida Song, Zhijun Wang, Wujun Shi, Gang Li, Chen Fang, and B. Andrei Bernevig, "All Magic Angles in Twisted Bilayer Graphene are Topological," Phys. Rev. Lett. **123**, 36401 (2019), arXiv:1807.10676.

[17] Stephen Carr, Shiang Fang, Pablo Jarillo-Herrero, and Efthimios Kaxiras, "Pressure dependence of the magic twist angle in graphene superlattices," Phys. Rev. B **98**, 085144 (2018), arXiv:1806.05078.

[18] Chuan Chen, A. H. Castro Neto, and Vitor M. Pereira, "Correlated states of a triangular net of coupled quantum wires: Implications for the phase diagram of marginally twisted bilayer graphene," Phys. Rev. B **101**, 165431 (2020), arXiv:1907.11450.

[19] Tommaso Cea, Niels R. Walet, and Francisco Guinea, "Electronic band structure and pinning of fermi energy to van hove singularities in twisted bilayer graphene: A self-consistent approach," Phys. Rev. B **100**, 205113 (2019).

[20] Hoi Chun Po, Haruki Watanabe, and Ashvin Vishwanath, "Fragile Topology and Wannier Obstructions," Phys. Rev. Lett. **121** (2018), 10.1103/PhysRevLett.121.126402, arXiv:1709.06551.

[21] Mikito Koshino, Noah F.Q. Yuan, Takashi Koretsune, Masayuki Ochi, Kazuhiko Kuroki, and Liang Fu, "Maximally Localized Wannier Orbitals and the Extended Hubbard Model for Twisted Bilayer Graphene," Phys. Rev. X **8**, 031087 (2018).

[22] Hoi Chun Po, Liujun Zou, T. Senthil, and Ashvin Vishwanath, "Faithful tight-binding models and fragile topology of magic-angle bilayer graphene," Phys. Rev. B **99**, 195455 (2019), arXiv:1808.02482.

[23] Dante M. Kennes, Johannes Lischner, and Christoph Karrasch, "Strong correlations and d+ id superconductivity in twisted bilayer graphene," Phys. Rev. B **98**, 241407 (2018), arXiv:1805.06310.

[24] Teemu J. Peltonen, Risto Ojajärvi, and Tero T. Heikkilä, "Mean-field theory for superconductivity in twisted bilayer graphene," Phys. Rev. B **98**, 220504 (2018), arXiv:1805.01039.

[25] Hiroki Isobe, Noah F.Q. Yuan, and Liang Fu, "Unconventional Superconductivity and Density Waves in Twisted Bilayer Graphene," Phys. Rev. X **8**, 041041 (2018), arXiv:1805.06449.

[26] M. J. Calderón and E. Bascones, "Interactions in the 8-orbital model for twisted bilayer graphene," Phys. Rev. B **102**, 155149 (2020).

[27] Tommaso Cea and Francisco Guinea, "Band structure and insulating states driven by coulomb interaction in twisted bilayer graphene," Phys. Rev. B **102**, 045107 (2020).

[28] Ting Fung Chung, Yang Xu, and Yong P. Chen, "Transport measurements in twisted bilayer graphene: Electron-phonon coupling and Landau level crossing," Phys. Rev. B **98**, 035425 (2018), arXiv:1805.01454.

[29] Matthew Yankowitz, Shaowen Chen, Hryhoriy Polshyn, Yuxuan Zhang, K. Watanabe, T. Taniguchi, David Graf, Andrea F. Young, and Cory R. Dean, "Tuning superconductivity in twisted bilayer graphene," Science (80-.). **363**, 1059–1064 (2019), arXiv:1808.07865.

[30] Xiaobo Lu, Petr Stepanov, Wei Yang, Ming Xie, Mohammed Ali Aamir, Ipsita Das, Carles Urgell, Kenji Watanabe, Takashi Taniguchi, Guangyu Zhang, Adrian Bachtold, Allan H. MacDonald, and Dmitri K. Efetov, "Superconductors, orbital magnets and correlated states in magic-angle bilayer graphene," Nature **574**, 653–657 (2019), arXiv:1903.06513.

[31] Yuhang Jiang, Xinyuan Lai, Kenji Watanabe, Takashi Taniguchi, Kristjan Haule, Jinhai Mao, and Eva Y. Andrei, "Charge order and broken rotational symmetry in magic-angle twisted bilayer graphene," Nature **573**, 91–95 (2019), arXiv:1904.10153.

[32] Aaron L. Sharpe, Eli J. Fox, Arthur W. Barnard, Joe Finney, Kenji Watanabe, Takashi Taniguchi, M. A. Kastner, and David Goldhaber-Gordon, "Emergent ferromagnetism near three-quarters filling in twisted bilayer graphene," Science (80-.). **365**, 605–608 (2019), arXiv:1901.03520.

[33] Alexander Kerelsky, Leo J. McGilly, Dante M. Kennes, Lede Xian, Matthew Yankowitz, Shaowen Chen, K. Watanabe, T. Taniguchi, James Hone, Cory Dean, Angel Rubio, and Abhay N. Pasupathy, "Maximized electron interactions at the magic angle in twisted bilayer graphene," Nature **572**, 95–100 (2019), arXiv:1812.08776.

[34] Youngjoon Choi, Jeannette Kemmer, Yang Peng, Alex Thomson, Harpreet Arora, Robert Polski, Yiran Zhang, Hechen Ren, Jason Alicea, Gil Refael, Felix von Oppen, Kenji Watanabe, Takashi Taniguchi, and Stevan Nadj-Perge, "Electronic correlations in twisted bilayer graphene near the magic angle," Nat. Phys. **15**, 1174–1180 (2019), arXiv:1901.02997.

[35] Yonglong Xie, Biao Lian, Berthold Jäck, Xiaomeng Liu, Cheng Li Chiu, Kenji Watanabe, Takashi Taniguchi, B. Andrei Bernevig, and Ali Yazdani, "Spectroscopic signatures of many-body correlations in magic-angle twisted bilayer graphene," Nature **572**, 101–105 (2019), arXiv:1906.09274.

[36] S. L. Tomarken, Y. Cao, A. Demir, K. Watanabe, T. Taniguchi, P. Jarillo-Herrero, and R. C. Ashoori, "Electronic Compressibility of Magic-Angle Graphene Superlattices," Phys. Rev. Lett. **123** (2019), 10.1103/PhysRevLett.123.046601, arXiv:1903.10492.

[37] M. Serlin, C. L. Tschirhart, H. Polshyn, Y. Zhang, J. Zhu, K. Watanabe, T. Taniguchi, L. Balents, and A. F. Young, "Intrinsic quantized anomalous Hall effect in a moiré heterostructure," Science (80-.). **367**, 900–903 (2020), arXiv:1907.00261.

[38] M. Haule, E. Y. Andrei, and K. Haule, "The Mott-semiconducting state in the magic angle bilayer graphene," (2019), arXiv:1901.09852.

[39] Noah F.Q. Yuan and Liang Fu, "Model for the metal-insulator transition in graphene superlattices and beyond," Phys. Rev. B **98**, 045103 (2018), arXiv:1803.09699.

[40] S. H. Pan, J. P. O'Neal, R. L. Badzey, C. Chamon, H. Ding, J. R. Engelbrecht, Z. Wang, H. Eisaki, S. Uchida, A. K. Gupta, K. W. Ng, E. W. Hudson, K. M. Lang, and J. C. Davis, "Microscopic electronic inhomogeneity in the high-Tc superconductor Bi2Sr2CaCu2O8+x," Nature **413**, 282–285 (2001).

[41] Maxime Leroux, Vivek Mishra, Jacob P.C. Ruff, Helmut Claus, Matthew P. Smyliea, Christine Opagiste, Pierre Rodière, Asghar Kayani, G. D. Gu, John M. Tranquada, Wai Kwong Kwok, Zahirul Islam, and Ulrich Welp, "Disorder raises the critical temperature of a cuprate superconductor," Proc. Natl. Acad. Sci. U. S. A. **166**, 10691–10697 (2019), arXiv:1808.05984.

[42] Pilkyung Moon, Mikito Koshino, and Young Woo Son, "Quasicrystalline electronic states in 30° rotated twisted bilayer graphene," Phys. Rev. B **99**, 165430 (2019), arXiv:1901.04701.

[43] Moon Jip Park, Hee Seung Kim, and Sungbin Lee, "Emergent localization in dodecagonal bilayer quasicrystals," Phys. Rev. B **99**, 245401 (2019), arXiv:1812.09170.

[44] Wei Yao, Eryin Wang, Changhua Bao, Yiou Zhang, Kenan Zhang, Kejie Bao, Chun Kai Chan, Chaoyu Chen, Jose Avila, Maria C. Asensio, Junyi Zhu, and Shuyun Zhou, "Quasicrystalline 30º twisted bilayer graphene as an incommensurate superlattice with strong interlayer coupling," Proc. Natl. Acad. Sci. U. S. A. **115**, 6928–6933 (2018).

[45] Sung Joon Ahn, Pilkyung Moon, Tae Hoon Kim, Hyun Woo Kim, Ha Chul Shin, Eun Hye Kim, Hyun Woo Cha, Se Jong Kahng, Philip Kim, Mikito Koshino, Young Woo Son, Cheol Woong Yang, and Joung Real Ahn, "Dirac electrons in a dodecagonal graphene quasicrystal," Science (80-.). **361**, 782–786 (2018).

[46] Yixing Fu, Elio J. König, Justin H. Wilson, Yang Zhi Chou, and Jedediah H. Pixley, "Magic-angle semimetals," npj Quantum Materials (2020), 10.1038/s41535-020-00271-9.

[47] Hadi Z. Olyaei, Bruno Amorim, Pedro Ribeiro, and Eduardo V. Castro, "Ballistic charge transport in twisted bilayer graphene," (2020), arXiv:2007.14498.

[48] Biao Huang and W. Vincent Liu, "Moiré localization in two-dimensional quasiperiodic systems," Phys. Rev. B **100**, 144202 (2019).

[49] Attila Szabó and Ulrich Schneider, "Mixed spectra and partially extended states in a two-dimensional quasiperiodic model," Phys. Rev. B **101**, 14205 (2019), arXiv:1909.02048.

[50] M. Rossignolo and L. Dell'Anna, "Localization transitions and mobility edges in coupled Aubry-Andr\'e chains," Phys. Rev. B **99**, 54211 (2018), arXiv:1804.03086.

[51] See supplemental material, which includes Refs.[68,69], for: details on finite-size scaling method used for exact diagonalization results and additional information on these results; Results on band inversion; technical details on the computation of momentum-space inverse participation ratio; technical details and additional results on conductance.

[52] We also tested models with intralayer hoppings up to third nearest neighbors and observed that the results remained qualitatively unaffected up to the expected shift in the energy of the Dirac points and a slight change in the narrow band angle θ_{ft}.

[53] G. De Trambly Laissardière, D. Mayou, and L. Magaud, "Localization of dirac electrons in rotated graphene bilayers," Nano Letters (2010), 10.1021/nl902948m.

[54] G. Trambly De Laissardière, D. Mayou, and L. Magaud, "Numerical studies of confined states in rotated bilayers of graphene," Phys. Rev. B - Condens. Matter Mater. Phys. **86**, 125413 (2012), arXiv:1203.3144.

[55] M. Andelković, L. Covaci, and F. M. Peeters, "DC conductivity of twisted bilayer graphene: Angle-dependent transport properties and effects of disorder," Phys. Rev. Mater. **2**, 34004 (2018), arXiv:1705.05731.

[56] This method was originally proposed in Ref. [**?**]. See also Ref. [**?**] for an example of a recent application.

[57] It is important to advert that the study of momentum-space localization in finite systems requires closed boundary conditions, which motivates the construction of approximant structures previously described. For open boundaries, one-dimensional edge defects are sufficient to induce momentum-space delocalization even for commensurate structures.

[58] V. Hernandez, J. E. Roman, and V. Vidal, "SLEPc: A scalable and flexible toolkit for the solution of eigenvalue problems," ACM Trans. Math. Software **31**, 351 (2005).

[59] S. Balay, S. Abhyankar, M. F. Adams, J. Brown, P. Brune, K. Buschelman, L. Dalcin, A. Dener, V. Eijkhout, W. D. Gropp, D. Karpeyev, D. Kaushik, M. G. Knepley, D. A. May, L. C. McInnes, R. T. Mills, T. Munson, K. Rupp, P. Sanan, B. F. Smith, S. Zampini, H. Zhang, and H. Zhang, "PETSc Web page," https://www.mcs.anl.gov/petsc (2019).

[60] A. Wobst, G. L. Ingold, P. Hänggi, and D. Weinmann, "From ballistic motion to localization: A phase space analysis," Eur. Phys. J. B **27**, 11–14 (2002).

[61] In fact, L is the linear size of the rhombus used to compute $\mathcal{I}_k$, which is proportional to $N^{1/2}$: this size is what sets the resolution for the computation of $\mathcal{I}_k$, see SM [51] for details.

[62] Y. Y. Atas, E. Bogomolny, O. Giraud, and G. Roux, "Distribution of the ratio of consecutive level spacings in random matrix ensembles," Phys. Rev. Lett. **110** (2013), 10.1103/PhysRevLett.110.084101, arXiv:1212.5611.

[63] Hryhoriy Polshyn, Matthew Yankowitz, Shaowen Chen, Yuxuan Zhang, K. Watanabe, T. Taniguchi, Cory R. Dean, and Andrea F. Young, "Large linear-in-temperature resistivity in twisted bilayer graphene," Nat. Phys. **15**, 1011–1016 (2019), arXiv:1902.00763.

[64] Yuan Cao, Debanjan Chowdhury, Daniel Rodan-Legrain, Oriol Rubies-Bigorda, Kenji Watanabe, Takashi Taniguchi, T. Senthil, and Pablo Jarillo-Herrero, "Strange Metal in Magic-Angle Graphene with near Planckian Dissipation," Phys. Rev. Lett. **124**, 076801 (2020), arXiv:1901.03710.

[65] Hridis K. Pal, Stephen Spitz, and Markus Kindermann, "Emergent Geometric Frustration and Flat Band in Moiré Bilayer Graphene," Phys. Rev. Lett. **123**, 186402 (2019), arXiv:1803.07060.

[66] Cheng Shen, Na Li, Shuopei Wang, Yanchong Zhao, Jian Tang, Jieying Liu, Jinpeng Tian, Yanbang Chu, Kenji Watanabe, Takashi Taniguchi, Rong Yang, Zi Yang Meng, Dongxia Shi, and Guangyu Zhang, "Observation of superconductivity with Tc onset at 12K in electrically tunable twisted double bilayer graphene," (2019), arXiv:1903.06952.

[67] Xiaomeng Liu, Zeyu Hao, Eslam Khalaf, Jong Yeon Lee, Yuval Ronen, Hyobin Yoo, Danial Haei Najafabadi, Kenji Watanabe, Takashi Taniguchi, Ashvin Vishwanath, and Philip Kim, "Tunable spin-polarized correlated states in twisted double bilayer graphene," Nature **583**, 221–225 (2020), arXiv:1903.08130.

[68] Yuan Cao, Daniel Rodan-Legrain, Oriol Rubies-Bigorda, Jeong Min Park, Kenji Watanabe, Takashi Taniguchi, and Pablo Jarillo-Herrero, "Electric Field Tunable Correlated States and Magnetic Phase Transitions in Twisted Bilayer-Bilayer Graphene," (2019), 10.1038/s41586-020-2260-6, arXiv:1903.08596.

[69] Fengcheng Wu, Timothy Lovorn, Emanuel Tutuc, Ivar

Martin, and A. H. MacDonald, "Topological Insulators in Twisted Transition Metal Dichalcogenide Homobilayers," Phys. Rev. Lett. **122**, 086402 (2019).

[70] Lei Wang, En-Min Shih, Augusto Ghiotto, Lede Xian, Daniel A. Rhodes, Cheng Tan, Martin Claassen, Dante M. Kennes, Yusong Bai, Bumho Kim, Kenji Watanabe, Takashi Taniguchi, Xiaoyang Zhu, James Hone, Angel Rubio, Abhay Pasupathy, and Cory R. Dean, "Magic continuum in twisted bilayer WSe2," (2019), arXiv:1910.12147.

[71] Yi-Wen Liu, Ying Su, Xiao-Feng Zhou, Long-Jing Yin, Chao Yan, Si-Yu Li, Wei Yan, Sheng Han, Zhong-Qiu Fu, Yu Zhang, Qian Yang, Ya-Ning Ren, and Lin He, "Tunable lattice reconstruction, triangular network of chiral one-dimensional states, and bandwidth of flat bands in magic angle twisted bilayer graphene," Phys. Rev. Lett. **125**, 236102 (2020).

[72] Francisco Guinea and Niels R. Walet, "Continuum models for twisted bilayer graphene: Effect of lattice deformation and hopping parameters," Phys. Rev. B **99**, 205134 (2019).

[73] Nguyen N. T. Nam and Mikito Koshino, "Lattice relaxation and energy band modulation in twisted bilayer graphene," Phys. Rev. B **96**, 075311 (2017).

[74] Shankar Iyer, Vadim Oganesyan, Gil Refael, and David A. Huse, "Many-body localization in a quasiperiodic system," Phys. Rev. B **87**, 134202 (2013).

[75] Michael Schreiber, Sean S. Hodgman, Pranjal Bordia, Henrik P. Lüschen, Mark H. Fischer, Ronen Vosk, Ehud Altman, Ulrich Schneider, and Immanuel Bloch, "Observation of many-body localization of interacting fermions in a quasirandom optical lattice," Science **349**, 842–845 (2015), https://science.sciencemag.org/content/349/6250/842.full.pdf.

[76] J. H. Pixley, Justin H. Wilson, David A. Huse, and Sarang Gopalakrishnan, "Weyl Semimetal to Metal Phase Transitions Driven by Quasiperiodic Potentials," Phys. Rev. Lett. **120** (2018), 10.1103/PhysRevLett.120.207604, arXiv:1802.04270.

[77] Christoph W Groth, Michael Wimmer, Anton R Akhmerov, and Xavier Waintal, "Kwant: a software package for quantum transport," New Journal of Physics **16**, 063065 (2014).

[78] E. Abrahams, P. W. Anderson, D. C. Licciardello, and T. V. Ramakrishnan, "Scaling theory of localization: Absence of quantum diffusion in two dimensions," Phys. Rev. Lett. **42**, 673–676 (1979).

Supplemental Material for:
Incommensurability-induced sub-ballistic narrow-band-states in twisted bilayer graphene

S1. FINITE-SIZE SCALING METHOD FOR EXACT DIAGONALIZATION

As mentioned in the main text, in order to make a finite-size scaling analysis with our method, we need to slightly change the angle to work with incommensurate structures only. Here, we discuss this procedure in more detail.

We build structures characterized by the integers (m, r, n) (m and r being two coprime integers), with twist angles $\theta = \theta(m, r)$ given by

$$\cos\theta = \frac{3m^2 + 3mr + r^2/2}{3m^2 + 3mr + r^2}, \tag{S1}$$

number of sites $N = N(m, r, n)$ and number of moiré patterns, $N_M = N_M(n, r)$:

$$N_M = \begin{cases} n^2 r^2 & , \quad \mathrm{mod}\ (r, 3) \neq 0 \\ n^2 r^2/3 & , \mathrm{mod}(r, 3) = 0 \end{cases}. \tag{S2}$$

Our finite-size scaling procedure satisfies, for a set of $\mathcal{N}$ consecutive structure sizes, labelled by $i = 1, ..., \mathcal{N}$ and characterized by (m_i, r_i, n_i) with $\theta_i = \theta(m_i, r_i)$ and $N_i = N(m_i, r_i, n_i)$, such that:

- Every structure only contains one supercell ($n_i = 1$);

- $N_{i+1} > N_i$, with N the total system size (number of sites);

- $|\theta_{i+1} - \theta_i|/|\theta_i - \theta_{i-1}| < 1$;

- $|\theta_2 - \theta_1| \sim 10^{-5}\mathrm{rad}$.

In order to guarantee that the system's properties are not significantly affected by differences in the angles used for structures in the finite-size scaling analysis, we ensure that the variation in θ is sufficiently small. We give an example of a possible set of structures in Fig. S1. In Fig. S1(a), we plot all the commensurate structures that can be generated for the range of angles $\theta \in [1.084°, 1.095°]$ and $r \leq 21$. The different angles for a fixed r were obtained by varying m. Out of these, we chose the angles marked with horizontal lines for the finite-size scaling analysis. With this choice, we can increase the system size [Fig. S1(b)], and decrease the required change in θ at the same time. The structures in this example were used in the main text, in Fig. 2(d–f). The full variation in θ is below $10''$ (see Table S1).

S2. COMPLEMENTARY INFORMATION ON EXACT DIAGONALIZATION RESULTS

In Fig. 1 of the main text, we plotted $\mathcal{I}_k$ and r_{st} averaged over a fixed energy window containing the narrow-band. Here we instead follow one of the VHS (the one of larger energy), averaging over a small energy window δE around it. For the angle corresponding to the narrower band, $\delta E(\theta_{\mathrm{ft}}) = 2.5 \times 10^{-5}$. For other angles, $\delta E(\theta) = \delta E(\theta_{\mathrm{ft}})\Delta E(\theta)/\Delta E(\theta_{\mathrm{ft}})$, where $\Delta E(\theta)$ is the narrow-band's width for an angle θ. This accounts for the broadening of the DOS around the VHS when the narrow-band becomes wider. The results are in Fig. S2, where we can see that $r_{\mathrm{st}}(\theta)$ and $\mathcal{I}_k(\theta)$ become more peaked around $\theta = \theta_{\mathrm{ft}}$ than in Fig. 1 of the main text, as expected.
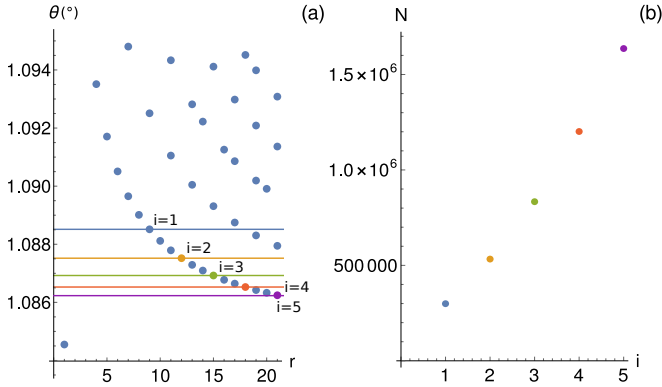
FIG. S1. (a) Full set of commensurate structures that can be generated for the range of angles $\theta \in [1.084°, 1.095°]$ and $r \leq 21$. The horizontal lines indicate a possible choice of a set of structures to make a finite-size scaling analysis. (b) Total system size N (number of sites) for the choice of structures in (a).
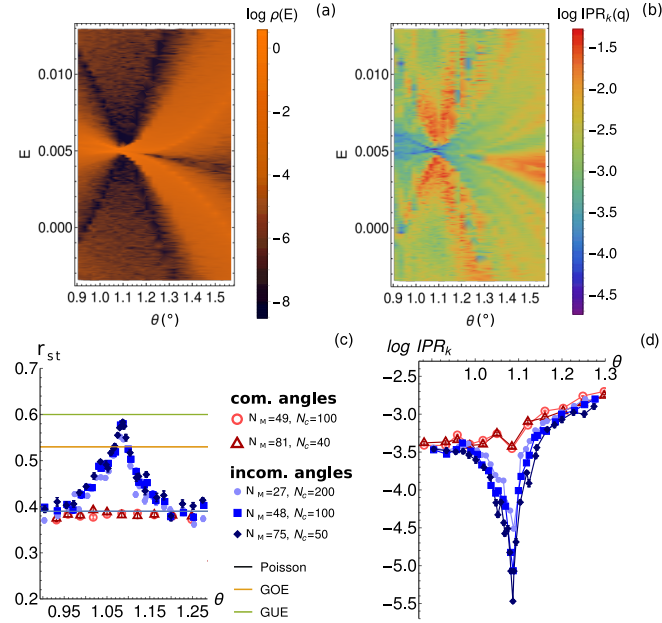

FIG. S2. Analogous of Fig. 1 of the main text. Panels (a,b) are the same as in Fig. 1 (reproduced here for clarity), while the results of panels (c,d) were instead obtained by following the VHS with higher energy. r_{st} and $\mathcal{I}_k$ were averaged in a small energy around it. For different angles, we rescaled the energy window used for averaging proportionally to the width of the narrow-band, as described in the text. The energy is in units of t.

In Fig. 2 of the main text, we analyzed sets of incommensurate angles for which the bandwidth becomes very narrow. In Fig. S3 we show a similar analysis for angles slightly above and below this regime. Note that even though sub-ballistic behavior ($|\partial \log \mathcal{I}_k / \partial \log L| > 0$ and $r_{st} > r_{st}^{Poisson}$) is generically observed, the large-L limiting behavior is not always clear. For instance, in
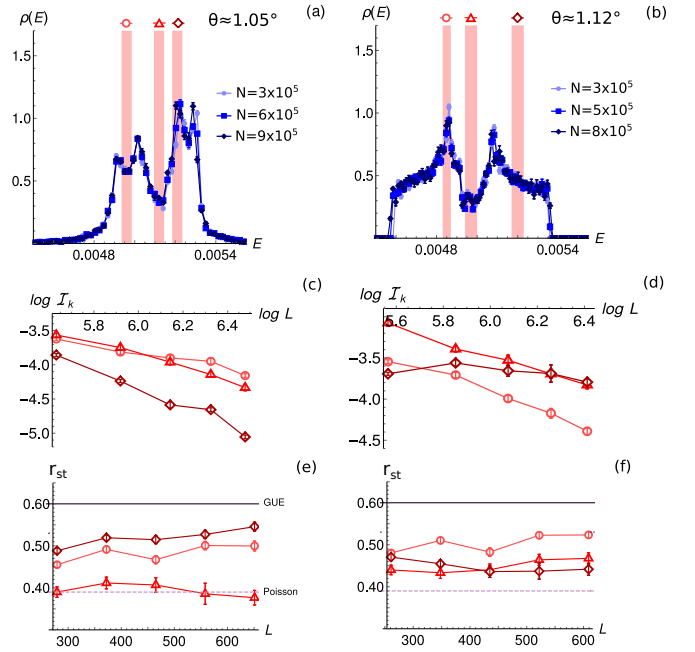

FIG. S3. (a,b) DOS for incommensurate structures of different sizes, for angles slightly below (a) and above (b) the narrow-band regime. (c-f) Average r and $\mathcal{I}_k$ for a small energy window around selected energies, depicted by the shaded areas in Figs. (a,b), as a function of the linear system size $L \propto N^{1/2}$ (the largest systems correspond to $N \gtrsim 10^6$). Above the shaded areas we show the plot markers used in the scaling analysis below the plots of $\rho(E)$ (in the same column). Complete information on the data used in Figs. (a-f) can be found in table S1. The energy is in units of t.

Fig. S3(f), we see that even though $r_{st} > r_{st}^{Poisson}$, it is not conclusive whether r_{st} will converge to r_{st}^{GUE} or $r_{st}^{Poisson}$ (or some intermediate value) upon increasing L.

We finish this section by providing detailed information on the data used in the plots of Fig. 2 and Fig. 3 of the main text and Fig. S3. Table S1 (S2) details the parameters used for calculations presented in Fig. 2 of the main text and Fig. S3 [Fig. 3(c-e) of the main text].

S3. BAND INVERSION

Fig. 1(a) of the main text raises the question on whether there is a band inversion as a function of θ.

To answer that, we can, similarly to Ref. [76], define projectors in both bands for a larger angle and project them into new states obtained upon decreasing the angle. The results evaluate the subspace with which the new states have the larger overlap. However, to use this method, the system sizes for different angles should be fixed. This is not achievable with our method of building the system.

An alternative way of observing the same angle-driven physics is by varying the interlayer coupling. Increasing

	(m,r)	$\theta(\approx)$	N	N_{M}	N_c
	(274,9)	1.0690	310 276	27	200
	(365,12)	1.0699	550 612	48	100
Fig. 2(a,c,e)	(457,15)	1.0682	863 116	75	50
	(547,18)	1.0709	1 236 652	108	25
	(638,21)	1.0712	1 682 356	147	25
	(269,9)	1.0885	299 236	27	200
	(359,12)	1.0875	532 948	48	100
Fig. 2(b,d,f)	(449,15)	1.0869	833 644	75	50
	(539,18)	1.0865	1 201 324	108	25
	(629,21)	1.0862	1 635 988	147	25
	(280,9)	1.0464	323 788	27	200
	(373,12)	1.0474	574 612	48	100
Fig. S3(a,c,e)	(466,15)	1.0479	896 884	75	50
	(559,18)	1.0483	1 290 604	108	25
	(652,21)	1.0485	1 755 772	147	25
	(262,9)	1.1171	284 116	27	200
	(349,12)	1.1182	504 148	48	100
Fig. S3(b,d,f)	(436,15)	1.1188	786 844	75	50
	(523,18)	1.1192	1 132 204	108	25
	(610,21)	1.1195	1 540 228	147	25

TABLE S1. Complete information on data used in Fig. 2 of the main text and Fig. S3. In the first column we only indicate (m,r) because $n=1$ (all structures are incommensurate). θ is the twist angle, N is the total number of sites in the system, N_{M} is the number of moiré patterns in the system and N_c is the total number of realizations (including averages over random twisted boundary conditions and shifts $\boldsymbol{\delta}_{\mathrm{t}}$). Each row corresponds to a point in Figs. 2(d,f) and Figs. S3(d,f). Note that in Fig. 2(a) and Fig. S3(a), the DOS is plotted for the three smallest system sizes used (first three rows in the corresponding section of the table).

	(m,r,n)	$\theta(\approx)$	N	N_{M}	N_c
	(7,1,25)		422 500	625	35
Fig. 3(c-e),com.	(7,1,30)	4.4085	608 400	900	24
	(7,1,35)		828 100	1225	18
	(7,1,40)		1 081 600	1600	13
	(190,27,1)	4.3868	165 892	243	102
	(232,33,1)	4.3907	247 372	363	68
	(274,39,1)	4.3934	345 076	507	49
Fig. 3(c-e),incom.	(316,45,1)	4.3954	459 004	675	36
	(358,51,1)	4.3970	589 156	867	28
	(400,57,1)	4.3982	735 532	1083	23
	(442,63,1)	4.3992	898 132	1323	18

TABLE S2. Complete information on data used in Figs. 3(c-e) of the main text, for the data points corresponding to commensurate and incommensurate structures. Each row corresponds to a point in Figs. 3(d,e). Note that in Fig. 3(c), the DOS is plotted for the smallest commensurate and incommensurate system size used (first row in the corresponding section of the table). See table S1 for description of the parameters.

the interlayer coupling for an angle above the narrow-band regime leads to similar results as decreasing the angle. The advantage is that the system size can be made fixed in the former.

We generalize the interlayer coupling $t_\perp(r)$ of the main text, defining a parameter V as

$$
t_\perp(V,r) = V\left(\frac{d_\perp^2}{d_\perp^2+r^2}V_{pp\sigma}\left(\sqrt{d_\perp^2+r^2}\right) + \frac{r^2}{d_\perp^2+r^2}V_{pp\pi}\left(\sqrt{d_\perp^2+r^2}\right)\right).
\tag{S3}
$$

We vary V for a fixed commensurate (incommensurate) angle $\theta\approx 1.2972°$ ($\theta\approx 1.2930°$) corresponding to the structure $(m,r)=(25,1)$ [$(m,r)=(301,12)$]. For $V=1$ we define the projector into the lowest and highest energy bands, respectively B_+ and B_- as

$$
P_\pm(V=1) = \sum_{v\in B_\pm}|v\rangle\langle v|,
\tag{S4}
$$

where $\{|v\rangle\}$ is the set of eigenstates obtained through exact diagonalization.

We then vary V and for each eigenstate $|v(V,E)\rangle$ in the energy window of interest we define the quantity

$$
\mathcal{C} = \langle v(V,E)|\left[P_+(V=1)-P_-(V=1)\right]|v(V,E)\rangle
\tag{S5}
$$

which should be $\mathcal{C}=1$ if $|v(V,E)\rangle$ belongs to B_+, $\mathcal{C}=-1$ if it belongs to B_- and $\mathcal{C}=0$ if it is orthogonal to both.

The results are in Fig. S4 for fixed configurations in the commensurate and incommensurate cases. In both cases, the results suggest that a band inversion occurs when the narrow-band regime is reached. The higher (lower) energy states for larger V (or equivalently, smaller θ) have a larger projection in B_- (B_+).
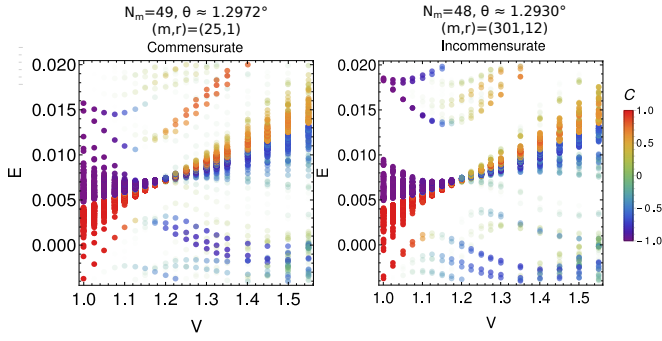
FIG. S4. Quantity $\mathcal{C}$ defined in Eq. S5 for every eigenstate within the energy window $E \in [0, 0.02]$, for variable V. The results were obtained for a fixed random twist and stacking, for the commensurate (incommensurate) structures $(m, r) = (25, 1)$ [$(m, r) = (301, 12)$]. The system sizes were chosen to contain $N_m = 48$ ($N_m = 49$) moiré patterns. The energy is in units of t.

S4. ROBUSTNESS OF INCOMMENSURABILITY EFFECTS TO DISORDER

In this section, we study how the effects presented in the main text are affected by the presence of disorder. In particular, we use disorder of the Anderson type, consisting of random on-site energies ϵ_i sampled according to a box distribution:

$$P_W(\epsilon_i) = \frac{1}{W}\Theta\left(\frac{W}{2} - |\epsilon_i|\right), \qquad (S6)$$

where W is the disorder strength and $\Theta(x)$ is the Heaviside function. We carried out an identical study to the one made in Fig. 1 of the main text for the clean case. In particular, we averaged $\mathcal{I}_k$ and r_{st} for the states within the same energy window used there ($E \in [0.004, 0.006]$). The results for different W are in Figs. S5, S6. We studied systems with $N_M = 48$ ($N_M = 49$) Moiré patterns for incommensurate (commensurate) angles. Similar system sizes were used for commensurate and incommensurate angles so that a fair comparison could be made. The reason follows: it is well known that any finite amount of disorder in 2D gives rise to real-space localization [78]. However, for the disorder strengths we are concerned with, the localization length is unrealistically large, much larger than the system sizes that we are studying and than the sample sizes that are studied experimentally. Still, different localization regimes may be reached for different system sizes and a fair comparison between commensurate and incommensurate strucutures should be made for similar system sizes.

The results in Figs. S5, S6 indicate that the differences observed between commensurate and incommensurate angles in the clean case are robust up to a relatively strong disorder, larger than the narrow-band's width (we define this width, NbW, as the smallest observed bandwidth, at $\theta = \theta_{\mathrm{ft}} \approx 1.09°$). For stronger disorder strengths, the results obtained for commensurate angles approach the results obtained for incommensurate angles.

The results in this section have two important implications. Firstly, they show that the effects of incommensurability are comparable to the effects of a strong disorder, reinforcing their importance. Secondly, they provide yet another indication of the fragility of the results obtained for commensurate structures, that are much less robust to disorder than the results obtained for incommensurate structures. Both points reinforce the importance of incommensurate structures to the physics of tBLG.
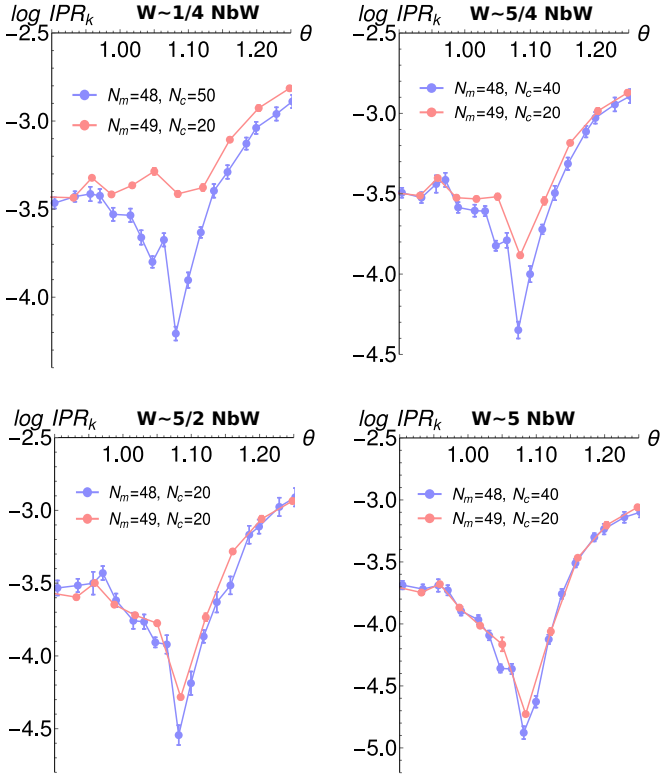
FIG. S5. $\mathcal{I}_k$ for commensurate (red points) and incommensurate (blue points) angles and variable disorder strength W. NbW is the smallest observed bandwidth, $\Delta E \approx 0.0004$, at $\theta = \theta_{\mathrm{ft}} \approx 1.09°$. The results were obtained for a fixed number of Moiré patterns, $N_M = 48$ ($N_M = 49$) for incommensurate (commensurate) angles.

FIG. S6. r_{st} for commensurate (red points) and incommensurate (blue points) angles and variable disorder strength W. NbW is the smallest observed bandwidth, $\Delta E \approx 0.0004$, at $\theta = \theta_{\mathrm{ft}} \approx 1.09°$. The results were obtained for a fixed number of Moiré patterns, $N_M = 48$ ($N_M = 49$) for incommensurate (commensurate) angles.

S5. TECHNICAL DETAILS ON THE COMPUTATION OF $\mathcal{I}_k$

We made use of the Fast Fourier Transform (FFT) method to compute the wavefunction in the momentum-space. We do this only for the unrotated layer (layer 1) without loss of generality: there is no "preferred" layer in our model and therefore the wavefunction is similar in both.

We cut a rhombus of linear size $L \propto N^{1/2}$ along the directions of the lattice vectors of the honeycomb lattice. L sets the momentum-space resolution for computing $\mathcal{I}_k$. In the main text, we always use the definition of L given here, for consistency. The total number of sites N is slightly larger than $4L^2$. Nonetheless, L can be seen as the total linear system size for all the discussions in the main text.

After cutting the smaller rhombus, we apply the FFT to the real-space wavefunction in that rhombus and finally compute $\mathcal{I}_k$ using the resulting momentum-space wavefunction.

An example of this procedure is in Fig. S7 for a structure with $(m, r, n) = (5, 3, 8)$. We notice that the ratio
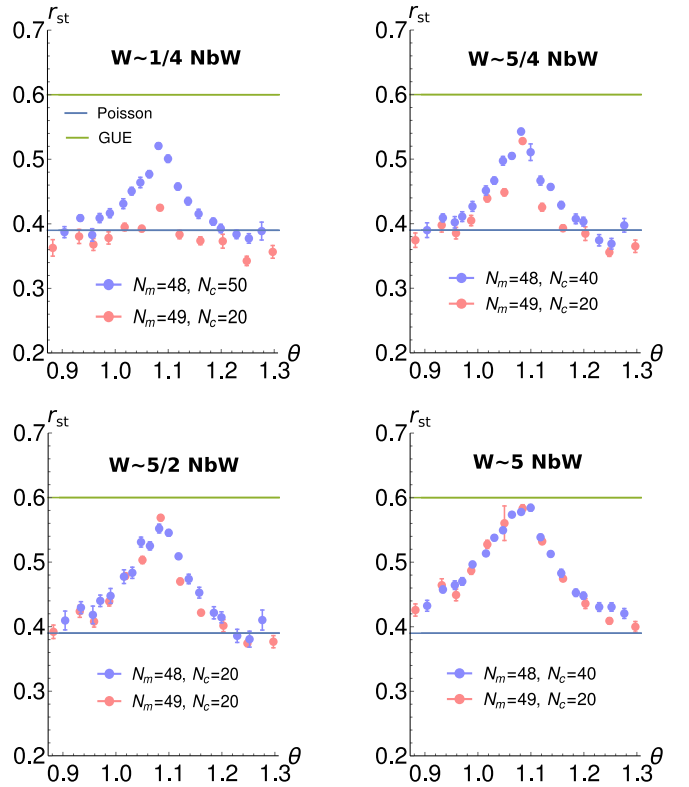
between the rhombus size and total system size becomes larger when we use structures with $\mathrm{mod}\,(r, 3) = 0$. For this reason we use structures of this type in the main text, but the obtained results are also valid for incommensurate structures with $\mathrm{mod}\,(r, 3) \neq 0$.

S6. TECHNICAL DETAILS ON CONDUCTANCE CALCULATIONS AND ADDITIONAL RESULTS

Conductance calculations were perfomed for the system depicted in Fig. S8: a parallelogramical tBLG scattering region, with a side of W and a base of L, with semi-infinite monolayer graphene leads attached to the bottom layer of the tBLG. In order to avoid the overlap in energy of the leads Dirac points (with a vanishing DOS) with the tBLG narrow-bands, we considered doped leads, with the left(right) lead shifted in energy by positive(negative) on-site potentials of $0.15t$, with respect to the tBLG region. The conductance, at zero temperature and in the linear regime, was computed within the Landauer approach. The conductance per width is given by $G = G_0 T\,(\epsilon)\,/W$, where $G_0 = 2e^2/h$ is the conductance quantum and $T\,(\epsilon)$
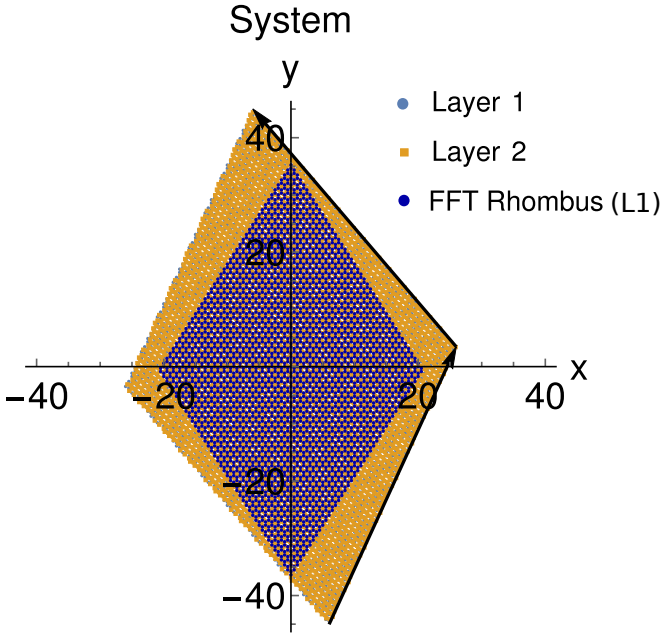
FIG. S7. Example structure $(m, r, n) = (5, 3, 8)$. The arrows correspond to $8\boldsymbol{v}_1$ and $8\boldsymbol{v}_2$, where $\boldsymbol{v}_1, \boldsymbol{v}_2$ are the superlattice vectors of the supercell defined by $(m, r) = (5, 3)$. In darker blue we represent the smaller rhombus selected in the unrotated layer (layer 1) for which we apply a Fast Fourier Transform in order to compute $\mathcal{I}_k$.

FIG. S9. Conductance results for $t_\perp = 0.48$eV in the narrow-band regime, for two close commensurate and incommensurate angles. Commensurate angle: $\theta \approx 1.0845, (m, r) = (30, 1)$ (blue diamonds); Incommensurate angle: $\theta \approx 1.0888, (m, r) = (29881, 1000)$ (red circles). This angle has a unit cell with approximately 10^{10} sites, much larger than the simulated system sizes. The energy is in units of t.
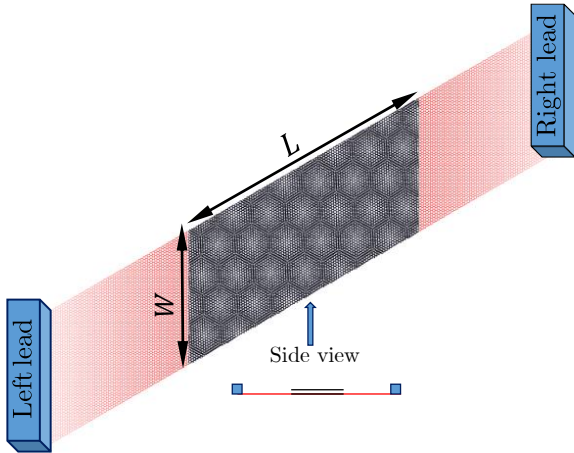

FIG. S8. Two-terminal conductance setup used in this work. The scattering region, in black, is tBLG of parallelogram shape. The leads are semi-infinite finite-width graphene ribbons. The side-view of the setup depicts that the tBLG region is connected to the leads through the bottom layer.

is the transmission at energy ϵ. The transmission was computed using the Kwant package [77]. The structures simulated have a width of $W = 1200a$, where a is the lattice constant of graphene, and contain from 0.8×10^6 up to 6.2×10^6 carbon atoms for increasing lengths, L, of the tBLG region. For each system size, G was averaged over 25 different stackings in tBLG region, where the cen-
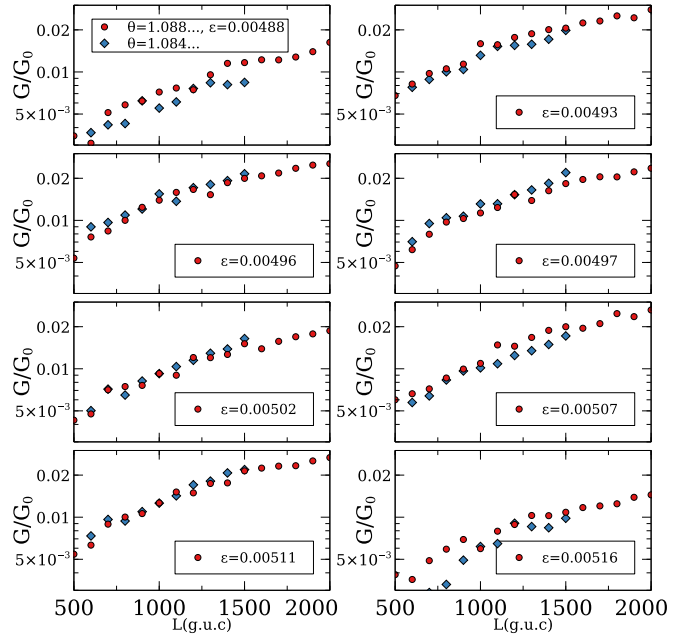
ter of rotation of the top layer is shifted with respect to the bottom layer along the vectors $\boldsymbol{\delta}_t = x\mathbf{a}_1 + y\mathbf{a}_2$, with $x, y \in \{0, 1/4, 2/4, 3/4, 1\}$ and $\mathbf{a}_{1/2}$ the primitive vectors of the top layer.

For the realistic tight binding model considered in the main text, where $t_\perp = 0.48$ eV, we computed G for both commensurate and incommensurate angles in the narrow-band regime, obtaining very similar results (see Fig. S9). Furthermore, $G(L)$ increases with L up to the maximal system size we were able to simulate. Note that for ballistic transport we expect an L-independent conductance, whereas $G(L) \propto L^{-1}$ for diffusion. Therefore, an increasing $G(L)$ with L implies that finite size effects are too severe to draw any conclusions. Such finite-size effects are not surprising as even the largest systems simulated contain only $N_M \sim 10^2$ moiré pattern cells.

To reduce finite-size effects, we considered a model with an increased interlayer coupling of $t_\perp = 1.9$ eV. For this increased interlayer hopping, the narrow-bands occur for $\theta_{\rm ft} \sim 4.4°$. Thus, the maximum size numerically attainable will include significantly more moiré pattern cells and finite-size effects are reduced. For this modified model, the number of moiré pattern cells in the scattering region ranges from $\gtrsim 2.8 \times 10^3$, for the smallest system size, up to $\gtrsim 2.1 \times 10^4$, for the largest system size simulated. $G(L)$ was again computed for two close commensurate and incommensurate angles in the new

narrow-band regime, $\theta_{\text{ft}} \sim 4.4°$, with the results shown in Fig. 3(a,b) of the main text.

To complement the conductance results in the main text, we show in Fig. S10 the conductance as a function of energy for additional commensurate and incommensurate twist angles close to the narrow-band regime, together with an ED analysis. With the ED analysis (first three rows) we show that similarly to the case of a smaller $t_{\perp}$, different scaling behaviours can be observed for different energies within the narrow-band regime. In the last row, we show the conductance as a function of energy for a fixed large system size and for commensurate and incommensurate angles close to the ones used in the ED analysis. We see that the conductance is smaller for an incommensurate angle in comparison with a nearby commensurate angle around energies for which the $\mathcal{I}_k$ scales faster with system size and r_{st} is closer to r_{GUE}. For such energies, the conductance for incommensurate angles is expected to decrease even more if larger systems are considered.
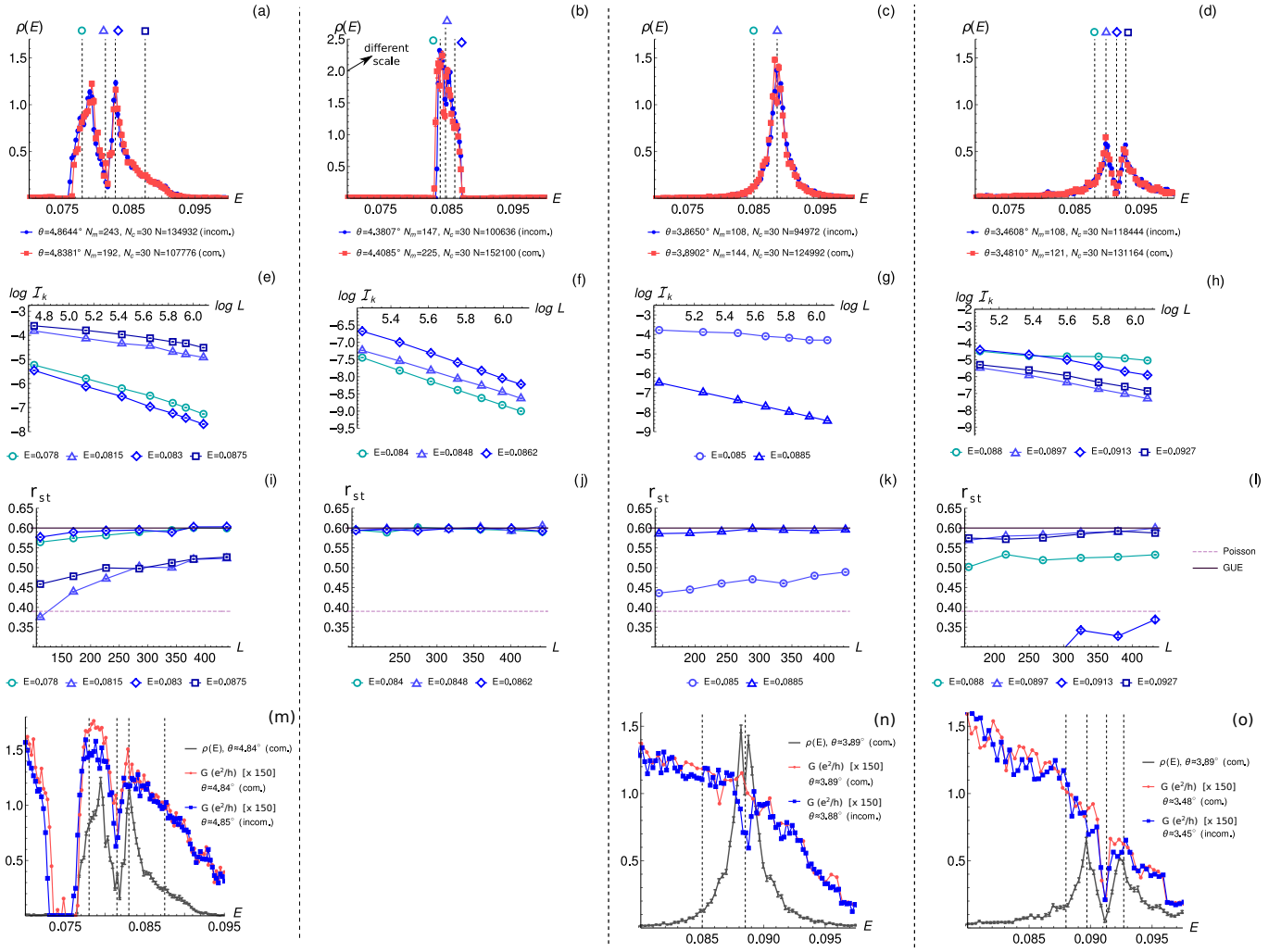
FIG. S10. (a-d) DOS for commensurate (full red squares) and incommensurate (full blue circles) structures around the narrow-band regime. For each column, we present results for two close commensurate and incommensurate angles. N_{M}, N_c, and N are respectively the number of moiré pattern cells, configurations and total number of sites in the system. (e-l) We make a finite-size scaling analysis for a set of incommensurate angles close to the angles depicted in (a-d), and plot the average $\mathcal{I}_k$ [panels (e-h)] and r_{st} [panels (i-l)] below the respective figure in the first row [panels (a-d)]. The average is taken over a small energy window around some selected energies, depicted by the dashed lines in panels. (a-d). Above these dashed lines we show the plotmarkers used in the corresponding scaling analysis in panels (e-l). Note that the scalings in each column are relative to the upper row figure in the same column. (m-o) Conductance, $G(e^2/h)$, as a function of energy for the commensurate angles used in the upper panels and for incommensurate angles close to them. The system sizes were fixed to $L = 3000$. To simulate the incommensurate angles, structures with a unit cell much larger than the system size were considered. The DOS for the commensurate angles is also shown in gray [for the incommensurate angles, the results are very similar, as shown in panels (a,b,d)]. The energy is in units of t.